

Centimetre-scale perovskite solar cells with fill factors above 86 per cent

Jun Peng^{1*}, Felipe Kremer², Daniel Walter¹, Yiliang Wu¹, Yi Ji³, Jin Xiang³, Wenzhu Liu⁴,
The Duong¹, Heping Shen¹, Teng Lu⁵, Frank Brink², Dingyong Zhong³, Li Li⁶, Olivier Lee
Cheong Lem⁶, Yun Liu⁵, Klaus J. Weber¹, Thomas P. White^{1*} & Kylie R. Catchpole^{1*}

¹School of Engineering, The Australian National University, ACT 2600, Australia.

²Centre for Advanced Microscopy, The Australian National University, ACT, 2600, Australia.

³State Key Laboratory of Optoelectronics Materials and Technologies, Sun Yat-sen University, Guangzhou 510275, China.

⁴Research Center for New Energy Technology, Shanghai Institute of Microsystem and Information Technology, Chinese Academy of Sciences, Jiading, Shanghai 201800, China.

⁵Research School of Chemistry, The Australian National University, ACT 2600, Australia.

⁶Australian National Fabrication Facility, Research School of Physics, The Australian National University, ACT 2600, Australia.

*Correspondence to: jun.peng@anu.edu.au (J.P.); thomas.white@anu.edu.au (T.P.W.); kylie.catchpole@anu.edu.au (K.R.C.)

Rapid development of both efficiency¹ and stability² mean that perovskite solar cells are at the forefront of emerging photovoltaic technologies. State-of-the-art cells exhibit voltage losses³⁻⁸ approaching the theoretical minimum and near-unity internal quantum efficiency⁹⁻¹³, but conversion efficiencies are limited by the fill-factor (FF < 83%, below the Shockley-Queisser limit of ~90%). This limitation results from non-ideal charge transport between the perovskite absorber and the cell's electrodes^{5,8,13-16}. Reducing the electrical series resistance of charge transport layers is therefore crucial for improving efficiency. Here we introduce a reverse-doping process to fabricate nitrogen-doped titanium oxide electron transport layers with outstanding charge transport performance. By incorporating this charge transport material into perovskite solar cells, we demonstrate 1cm² cells with FFs >86%, and an average FF ~ 85.3%. We also report a certified steady-state efficiency record of 22.6% for a 1cm² cell (23.33% ± 0.58% from reverse current-voltage scan).

Nitrogen-doped titanium oxide (titanium oxynitride, TiO_xN_y) has been widely investigated for photocatalysis^{17,18}, but rarely in perovskite solar cells (PSCs). PSCs incorporating solution-processed TiO_xN_y have been reported, but device performances have

not exceeded that of PSCs with standard TiO_x electron transport layers (ETLs)^{19,20}, because the stoichiometric control required to optimise metal oxide transport layer properties is challenging with solution processing. Instead, we report here a reverse doping method to produce high quality TiO_xN_y films by oxidising sputtered titanium nitride thin films using a controlled annealing temperature in an oxygen atmosphere (details are provided in Methods). In addition to producing high quality TiO_xN_y films, sputtering is already widely used in the photovoltaic and electronics industries and is therefore a promising deposition method for commercial fabrication of perovskite solar cells.

TiO_xN_y film composition and morphology

To understand the impact of the annealing process on the physical and electronic properties of TiO_xN_y , we prepared films (thickness ~50 nm) with seven different annealing conditions: ‘as-deposited’ (room temperature), ‘300 C’, ‘350 C’ ‘400 C’ ‘450 C’, ‘500 C’ and ‘550 C’. There is no significant difference in the morphology of the resulting TiO_xN_y films (Extended data Fig. 1), and they are similar to the bare fluorine doped tin oxide (FTO) coated glass substrates.

We next investigate the elemental composition of TiO_xN_y using x-ray photoelectron spectroscopy (XPS). As shown in Fig. 1a, the Ti^{2+} oxidation state²¹ is present in the as-deposited TiN film as evidenced by the presence of O 1s^{15,22} (Fig. 1b) and O-Ti-N^{18,23,24} XPS peaks (Fig. 1c). The appearance of Ti^{3+} and Ti^{4+} states after annealing at 300°C indicates partial oxidation of the TiN, and oxidation increases at higher temperatures. For samples annealed at 450°C and above, only the highest Ti^{4+} oxidation state is present^{15,21}. Meanwhile, the $\text{TiN}^{18,23}$ peak weakens and eventually disappears at higher annealing temperatures, and two new N 1s core-level peaks ($\text{NO}_x^{18,23,25}$ and $\gamma\text{-N}_2^{23,26}$ (chemisorbed N_2)) are observed (Fig. 1c). This further demonstrates that the chemical states of Ti and N within TiO_xN_y lattices continuously changes as the oxidation temperature increases. More details of the XPS analysis can be found in Methods.

By combining the elements’ relative peak areas and sensitivity factors (Extended data Fig. 2), we calculate that the atomic ratio of O:Ti (N:Ti) is 0.58 (0.62) for the ‘as-deposited’ film. The O:Ti atomic ratio increases with annealing temperature, reaching a peak of 2.24 at 500°C before decreasing. In contrast, the N:Ti ratio decreases monotonically with annealing temperature. However, N atoms remain in the TiO_xN_y film at higher temperatures, with N:Ti ratios of 0.08 and 0.07 for samples annealed at 500°C and 550°C respectively.

High resolution transmission electron microscopy (TEM) imaging (Extended data Fig. 3a) shows that the ‘as-deposited’ film is not completely crystalline and features an amorphous contrast along with a distribution of crystalline particles with characteristic sizes ranging from 10 nm to 20 nm. A survey of the first two diffraction rings from the polycrystalline pattern in Fig. 2a reveals diffracting planes corresponding to distances of $d_1 = 2.45 \pm 0.07 \text{ \AA}$ and $d_2 = 2.12 \pm 0.06 \text{ \AA}$, which can be respectively assigned to the cubic phases of TiO^{27} and TiN^{27} ($d_{(111),\text{TiO}} = 2.411 \text{ \AA}$, $d_{(200),\text{TiO}} = 2.088 \text{ \AA}$; $d_{(111),\text{TiN}} = 2.445 \text{ \AA}$, $d_{(200),\text{TiN}} = 2.117 \text{ \AA}$). Detailed parameters for simulation are summarised in Supplementary Table S1. Given the XPS result which shows a large concentration of N relative to O, and the difficulty of differentiating the cubic TiO from the cubic TiN (Extended data Fig.2), we conclude that the observed crystalline phase has a composition of the type TiO_xN_y . Similar analysis of the ‘300 C’, ‘350 C’ and ‘400 C’ films indicates that these are also largely composed of the cubic TiO_xN_y phase (Fig. 2 and Extended data Fig. 4). Note that there are two rings in the ‘400 C’ diffraction patterns (Fig. 2c) which can be allocated to the tetragonal anatase crystal phases of $\text{TiO}_x\text{N}_y^{28}$.

The combined evidence of the XPS and TEM analysis shows that oxidation at low temperatures ($<400^\circ\text{C}$) starts a restructuring process in which TiN and TiO crystals transform into amorphous TiO_xN_y , which then continues to form TiO_xN_y crystals under oxidation at high temperatures ($>450^\circ\text{C}$). Compared with the ‘as-deposited’, ‘300 C’, ‘350 C’ and ‘400 C’ cases, an increased crystalline fraction is observed for the TiO_xN_y film annealed at 450°C and above (Extended data Figs. 3 and 4). The ‘450 C’ diffraction patterns are dominated by a combination of tetragonal anatase and rutile phases of $\text{TiO}_x\text{N}_y^{28}$, accompanied by the complete disappearance of the cubic TiO_xN_y phase (Extended data Fig. 4d). At the highest temperature investigated, the ‘550 C’ film features large tetragonal crystals with sizes of over 20 nm with similar crystal phases to the ‘500 C’ film (Fig. 2d and Extended data Figs. 4e and 4f).

Optoelectronic properties of TiO_xN_y film

The as-deposited TiN film has a work function (WF) of $\sim 4.32 \text{ eV}$ (Fig. 3a) and an optical bandgap (E_g) of $\sim 3.25 \text{ eV}$ (Extended data Fig. 5), similar to literature values³². The WF of the ‘300 C’, ‘350 C’, ‘400 C’, ‘450 C’, ‘500 C’ and ‘550 C’ samples are 4.32 eV, 4.29 eV, 4.14 eV, 4.08 eV, 4.16 eV, 4.14 eV and 4.28 eV, respectively, which are associated with the free carrier density (or doping density) change and/or surface dipoles within the TiO_xN_y films. Figure 3b shows the energy level distribution of TiO_xN_y films for different annealing

temperatures, extracted by combining data from ultraviolet photoelectron spectroscopy (UPS) spectra (Fig. 3a) and E_g measurements (Extended data Fig. 5).

In addition to the WF change, the energy difference (ΔE) between Fermi level (E_f) and conduction band minimum (CBM) of TiO_xN_y increases with higher annealing temperatures. This indicates a reduction in free carrier density (or doping density) of the n-type TiO_xN_y which we quantify using Hall-effect measurements (Fig. 3c). The charge carrier density decreases steadily with increasing annealing temperatures up to 400°C, followed by a drop of approximately three orders of magnitude between the ‘400 C’ ($5.1 \times 10^{20}/\text{cm}^3$) and ‘450 C’ ($5.0 \times 10^{17}/\text{cm}^3$) samples. This coincides with the formation of the higher oxidation state of Ti, and loss of N from the TiO_xN_y lattice, as discussed previously. The carrier density decreases to $3.4 \times 10^{16}/\text{cm}^3$ when annealed at 550°C. Consequently, the conductivity of the films exhibits a similar trend to the free carrier density; the Hall mobility has an opposite trend (Fig. 3c). For comparison, we note that a control film made from solution-processed pure TiO_x ¹⁵ film annealed at 500°C has a much lower carrier density ($4.5 \times 10^{14}/\text{cm}^3$) and conductivity ($9.8 \times 10^{-5} \text{ S/cm}$) than both the ‘500 C’ and ‘550 C’ TiO_xN_y samples. The detailed Hall-effect results are summarised in Extended Data Table 1.

Despite the bandgap of the TiO_xN_y undergoing no significant change with annealing temperature (Extended data Fig.5), samples annealed at 400°C and below exhibit low optical transmittance across the visible spectrum (Fig 3d), which we attribute to strong free carrier absorption³³. A substantial increase in transmittance for films annealed at temperatures of 450°C and above coincides with the compositional, structural and electronic transition identified above. Thus, the combination of high conductivity and high optical transmittance for films annealed above 450°C indicates that TiO_xN_y films produced in this way have potential as high-performance ETLs for PSCs.

Solar cell characterisation

Having investigated the physical, electronic and optical properties of the TiO_xN_y films, we next investigate their use as ETLs in n-i-p PSCs. The devices studied here feature a structure of glass/FTO/ TiO_xN_y (~40 nm)/meso- TiO_2 (~50 nm)/PMMA:PCBM/ $\text{Cs}_{0.05}\text{FA}_{0.9}\text{MA}_{0.05}\text{PbI}_{2.74}\text{Br}_{0.26}$ (~500 nm)/PMMA/P3HT:CuPc (~65 nm)/Au (Fig. 4a and Extended data Fig. 6). Here, meso- TiO_2 represents mesoporous TiO_2 , PMMA⁵ and PMMA:PCBM⁵ are ultrathin interface passivation layers consisting of poly(methyl-methacrylate) and PMMA: ([6,6]-phenyl-C61-butyric-acid-methyl-ester) respectively, and P3HT:CuPc⁸ is a blended hole transport layer consisting of poly(3-

hexylthiophene) and copper phthalocyanine. Solution-processed compact TiO_x ¹⁵ substitutes TiO_xN_y as the ETL in the control cells.

As shown in Fig. 4a, our champion 1 cm^2 active area TiO_xN_y -based cell yielded a PCE of 23.36% (23.38%) with $V_{OC} \sim 1.193\text{ V}$ (1.200 V), $J_{SC} \sim 22.80\text{ mA/cm}^2$ (22.89 mA/cm^2) and FF ~ 0.859 (0.851) from reverse (forward) scan in-house measurements. The TiO_x -based control cell exhibited a maximum PCE of 21.65 % ($V_{OC} \sim 1.172\text{ V}$, $J_{SC} \sim 22.75\text{ mA/cm}^2$ and FF ~ 0.812) and 21.22% ($V_{OC} \sim 1.171\text{ V}$, $J_{SC} \sim 22.70\text{ mA/cm}^2$ and FF ~ 0.798) from reverse and forward scans, respectively. External quantum efficiency (EQE) spectra and perovskite optical bandgap ($E_g \sim 1.57\text{ eV}$) plots confirm the accuracy of the measured photocurrent as demonstrated by a discrepancy $<2\%$ between the integrated J_{SC} from the EQE spectra and the J_{SC} measured from the J - V curve (Fig. 4b). Another cell was submitted to an independent testing center and achieved a certified efficiency of $\sim 23.33\% \pm 0.58\%$ with a FF of $86.68\% \pm 1.01\%$ from reverse J - V scan, and a steady-state efficiency of $\sim 22.6\%$ (Supplementary Fig. 2). This is the highest certified efficiency for 1 cm^2 PSCs¹ and the highest FF reported for a PSC of any size (Supplementary Tables S4 and S5).

The J - V parameter distribution plots in Figs. 4c and Extended data Fig. 7a illustrate the reproducibility of our 1 cm^2 PSCs. The average PCE of the TiO_xN_y -based cells is $23.09\% \pm 0.11\%$ with an average FF $\sim 0.853 \pm 0.005$, while that of the TiO_x -based cells is $21.26\% \pm 0.33\%$ (average FF $\sim 0.793 \pm 0.014$). There is little difference in both V_{OC} and J_{SC} between the TiO_xN_y - and TiO_x -based cells (Extended data Fig. 7a), so the efficiency gains for TiO_xN_y -based cells are dominated by the higher FF which results from improved electron transport. A similar trend was also found between the TiO_xN_y - and TiO_x -based PSCs fabricated with indium tin oxide (ITO) coated glass substrates (see Supplementary Fig. 3, and discussion in the Methods section).

PSCs fabricated with TiO_xN_y ETLs annealed at 550°C exhibited a lower average PCE of $21.42\% \pm 0.32\%$ with substantial FF losses (Extended data Figs. 7b and 7c) compared to cells processed at 500°C . This is due to the order of magnitude reduction in carrier density in the ‘550 C’ sample compared to the ‘500 C’ sample.

We performed scanning electron microscopy (SEM), X-ray diffraction (XRD), and time-resolved photoluminescence (TRPL) measurements to investigate the effect of ETL composition on subsequently-deposited perovskite films. As seen in Supplementary Fig. 4, we found no evidence of changes in the surface morphology (from SEM images), nor in crystal structure, orientation or crystallinity (from XRD measurements) of perovskite films deposited on the different substrates. There was also little difference in the TRPL decay

measurements, consistent with the experimental cell V_{OC} values. This suggests that the very high FFs of the TiO_xN_y -based perovskite cells are derived from the improved electronic property of the TiO_xN_y film itself.

To explain how TiO_xN_y can significantly increase FF, we employed numerical one-dimensional, multilayer ionic-electronic numerical device simulations. Our focus is on the electrostatics of the perovskite/ETL/FTO layer structure. The empirical data suggests that increased dopant density is the only electronic factor that conclusively distinguishes TiO_xN_y from TiO_x . Yet a simple analytical treatment based on *ex-situ* conductivity of the ETL layers cannot explain the difference in FF. For 50 nm ETL layers, the optimum TiO_xN_y ($N_D = 3 \times 10^{17} \text{ cm}^{-3}$) reduces the voltage losses relative to TiO_x ($N_D = 5 \times 10^{14} \text{ cm}^{-3}$) by only ~3 mV at the maximum power point (MPP) current of 22 mA/cm^2 (where $\mu_e = 0.5 \text{ cm}^2 \text{ V}^{-1} \text{ s}^{-1}$). This is a small fraction of the experimental mean MPP voltage loss of approximately 80 mV. Instead, our model explains the resistance-related fill factor loss by showing that heavy doping of the ETL layer protects against electron depletion that can occur in regions of positive space charge at the perovskite/ETL and FTO/ETL heterojunctions. Equilibrium conditions in the perovskite/ETL/FTO structure depletes the ETL of electrons to concentrations that can be orders-of-magnitude below the fixed dopant density (Figure 4d). At the TiO_x dopant density of $5 \times 10^{14} \text{ cm}^{-3}$, the equilibrium free electron concentration can be closer to 10^{13} cm^{-3} , introducing many tens of mVs of voltage loss in the ETL at MPP currents (see Extended data Fig. 8 for details). Our simulations suggest that although modifications of the work function alignment between these materials, and in particular the ETL and FTO layer, can mitigate the effect to some extent, high doping ($\gtrsim 10^{17} \text{ cm}^{-3}$) in the ETL layer will, in general, be necessary (although not sufficient) to achieve PSC fill factors above approximately 85%.

We conclude this work by investigating the cell stability³⁴. As seen in Extended data Fig. 9a, the unencapsulated TiO_xN_y -based cell exhibited a steady-state PCE of ~22.82% after 250 hours of maximum power point voltage (V_{MPP}) tracking under continuous 1 sun illumination in nitrogen, retaining ~98.7% of its initial efficiency (~23.12%). Similarly, the TiO_x -based cell (~20.24%) retained ~96.5% of its initial efficiency (~20.97%), demonstrating no significant difference in light soaking stability between the unencapsulated cells with different ETLs (Extended data Fig. 9b). Two cells of each type were also subjected to damp-heat exposure in the dark. For these tests, an additional MoO_x (~10 nm)/IZO (~40 nm) barrier layer was deposited between the HTL and the gold electrode resulting in a reduced FF relative to the unencapsulated cells reported above. All four individual cells retained over 90% of their initial efficiencies after 1000 hours. Time-dependent power output and J - V curves are

presented in Supplementary Figs. 5 and 6 showing the cell performance evolution during the degradation tests. Although both the light soaking and damp-heat stability tests show promising results, these are not sufficient to guarantee the stability of perovskite cells under real operating conditions where thermal, light and humidity stressors act simultaneously³⁴. According to the literature^{2,35}, the combination of these conditions can accelerate degradation of the perovskite active layer, even in the presence of stable charge transport layers and encapsulation. As the perovskite used in this work was not optimized to withstand such conditions, a more stable composition such as those reported in Ref [2,35] would be necessary to realise the full benefits of the TiO_xN_y ETL.

References

1. Green, A. M. et al. Solar cell efficiency tables (version 57). *Prog. Photovolt. Res. Appl.* **29**, 3-15 (2021).
2. Bai, S. et al. Planar perovskite solar cells with long-term stability using ionic liquid additives. *Nature* **571**, 245-250 (2019).
3. Saliba, M. et al. Incorporation of rubidium cations into perovskite solar cells improves photovoltaic performance. *Science* **354**, 206-209 (2016).
4. Correa-Baena, J.-P. et al. Identifying and suppressing interfacial recombination to achieve high open-circuit voltage in perovskite solar cells. *Energy Environ. Sci.* **10**, 1207-1212 (2017).
5. Peng, J. et al. A universal double-side passivation for high open-circuit voltage in perovskite solar cells: role of carbonyl groups in poly(methyl methacrylate). *Adv. Energy Mater.* **8**, 1801208 (2018).
6. Luo, D. et al. Enhanced photovoltage for inverted planar heterojunction perovskite solar cells. *Science* **360**, 1442-1446 (2018).
7. Yang, S. et al. Tailoring passivation molecular structure for extremely small open-circuit voltage loss in perovskite solar cells. *J. Am. Chem. Soc.* **141**, 5781-5787 (2019).
8. Peng, J. et al. Nanoscale localized contacts for high fill factors in polymer-passivated perovskite solar cells. *Science* **371**, 390-395 (2021).
9. Kim, M. et al. Methylammonium chloride induces intermediate phase stabilization for efficient perovskite solar cells. *Joule* **3**, 2179-2192 (2019).
10. Min, H. et al. Efficient, stable solar cells by using inherent bandgap of α -phase formamidinium lead iodide. *Science* **366**, 749-752 (2019).

11. Zhu, H. et al. Tailored amphiphilic molecular mitigators for perovskite solar cells with 23.5% efficiency. *Adv. Mater.* **32**, 1907757 (2020).
12. Jiang, Q. et al. Surface passivation of perovskite film for efficient solar cells. *Nat. Photonics* **13**, 460-466 (2019).
13. Jung, E. H. et al. Efficient, stable and scalable perovskite solar cells using poly(3-hexythiophene). *Nature* **567**, 511-515 (2019).
14. Giordano, F. et al. Enhanced electronic properties in mesoporous TiO₂ via lithium doping for high-efficiency perovskite solar cells. *Nat. Commun.* **7**, 10379 (2016).
15. Peng, J. et al. Efficient indium-doped TiO_x electron transport layers for high-performance perovskite solar cells and perovskite-silicon tandems. *Adv. Energy Mater.* **7**, 1601768 (2017).
16. Zhou, H. et al. Interface engineering of highly efficient perovskite solar cells. *Science* **345**, 542-546 (2014).
17. Asahi, R., Morikawa, T., Ohwaki, T., Aoki, K. & Taga, Y. Visible-light photocatalysis in nitrogen-doped titanium oxides. *Science* **293**, 269-271 (2001).
18. Asahi, R., Morikawa, T., Irie, H. & Morikawa, T. Nitrogen-doped titanium dioxides as visible-light-sensitive photocatalyst: design, development, and prospects. *Chem. Rev.* **114**, 9824-9852 (2014).
19. Shasti, M. & Mortezaali, A. The effect of nitrogen doping of TiO₂ compact blocking layers on perovskite solar cell performance. *Solid States Sci.* **92**, 68-75 (2019).
20. Zhang, Z. et al. Enhancement of perovskite solar cells efficiency using N-doped TiO₂ nanorod arrays as electron transfer layer. *Nanoscale Res. Lett.* **12**, 43 (2017).
21. NIST X-ray photoelectron spectroscopy database. NIST standard reference database number 20, National Institute of Standards and Technology, Gaithersburg MD, 20899 (2000). doi:10.18434/T4T88K.
22. Shahiduzzaman, Md. et al. Low-temperature processed TiO_x electron transport layer for efficient planar perovskite solar cells. *Nanomaterials* **10**, 1676 (2020).
23. Zhang, L. et al. N-TiO₂-coated polyester filters for visible light—Photocatalytic removal of gaseous toluene under static and dynamic flow conditions. *J. Environ. Chem. Eng.* **4**, 357-364 (2016).
24. Batzill, M., Morales, E. H. & Diebold U. Influence of Nitrogen Doping on the Defect Formation and Surface Properties of TiO₂ Rutile and Anatase. *Phys. Rev. Lett.* **96**, 026103 (2006).
25. Napoli, F. et al. The nitrogen photoactive centre in N-doped titanium dioxide formed via

- interaction of N atoms with the solid. Nature and energy level of the species. *Chem. Phys. Lett.* **477**, 135-138 (2009).
26. Milošv, I., Strehblow, H.-H., Navinšek, B. & Metikoš-Huković, M. Electrochemical and thermal oxidation of TiN coatings studied by XPS. *Surf. Interface Anal.* **23**, 529-539 (1995).
27. Wyckoff, R. W. G. Crystal Structures 1. 85-237 (1963), Interscience Publishers, New York, USA.
28. Howard, C. J., Sabine, T. M. & F. Dickson, F. Structural and thermal parameters for rutile and anatase. *Acta Cryst.* **B47**, 462-468 (1991).
29. Hanaor, D. A. & Sorrell, C. C. Review of the anatase to rutile phase transformation. *J. Mater. Sci.* **46**, 855-874 (2011).
30. Brudnik, A., Bucko, M., Radecka, M., Trenczek-Zajac, A. & Zakrzewska, K. Microstructure and optical properties of photoactive TiO₂:N thin films. *Vacuum* **82**, 936-941 (2008).
31. Morikawa, T., Asahi, R., Ohwaki, T., Aoki, K. & Taga, Y. Band-gap narrowing of titanium dioxide by nitrogen doping. *Jpn. J. Appl. Phys.* **40**, L561-L563 (2001).
32. Yang, X. et al. Dual-function electron-conductive, hole-blocking titanium nitride contacts for efficient silicon solar cells. *Joule* **3**, 1314-1327 (2019).
33. Peelaers, H., Kioupakis, E. & Van de Walle, C. G. Free-carrier absorption in transparent conducting oxides: phonon and impurity scattering in SnO₂. *Phys. Rev. B* **92**, 235201 (2015).
34. Khenkin, M. V. et al, Consensus statement for stability assessment and reporting for perovskite photovoltaics based on ISOS procedures. *Nat. Energy* **5**, 35-49 (2020).
35. Lin, Y.-H. et al, A piperidinium salt stabilizes efficient metal-halide perovskite solar cells. *Science* **369**, 96-102 (2020).

Fig. 1 | X-ray photoelectron spectroscopy characterization of TiO_xN_y films annealed at different temperatures. Evolution of the chemical state of **a**, Ti, **b**, O, and **c**, N in TiO_xN_y films under different oxidation conditions. Note that the Ti 2p peaks centered at binding energies of ~457.5 eV and ~463.4 eV and the N 1s peak centred at ~399.5 eV binding energy can be ascribed to the satellite features of TiN.

Fig. 2 | Transmission electron microscopy characterization and simulation of the diffraction pattern. **a**, TiO_xN_y without annealing ('as-deposited'). TiO_xN_y annealed at **b**, 300°C, **c**, 400°C, **d**, 500°C. The crystal phases of the TiO_xN_y annealed at 300 and 400°C are cubic TiO_xN_y mixtures. Note that it is unusual for the rutile phase of TiO_xN_y to form at the relatively low annealing temperature of 450°C. In contrast, solution-processed TiO_x forms an anatase phase when annealed at 500 and 550°C (Supplementary Fig. 1). Anatase is often the first TiO_x crystal phase to form in many fabrication processes, due to its low surface energy²⁹ even though it is not an equilibrium phase for TiO_x in terms of the lattice stability. It typically converts to rutile, a more thermally stable phase, at temperatures over 550°C²⁹. However, studies suggest that the phase transition temperature strongly depends on impurities (or dopants) as well as on the morphology of the sample²⁹⁻³¹. This may explain the formation of rutile TiO_xN_y phase in the '450 C' sample.

Fig. 3 | Optoelectronic properties of TiO_xN_y films annealed at different temperatures. **a**, Work function and valance band maximum (VBM) of TiO_xN_y films determined by UPS spectra. **b**, Energy level distribution of TiO_xN_y films. **c**, Carrier density, conductivity and Hall mobility of TiO_xN_y films. **d**, Optical transmittance of TiO_xN_y films (deposited on FTO substrates). Note that the VBM is determined by the sum of WF and ($E_f - E_v$); while the CBM is determined by VBM - E_g . The detailed data of the UPS and Hall-Effect measurements are also provided in Supplementary Table S2 and S3, respectively.

Fig. 4 | Device characterization and simulation. **a**, J - V curves of the champion 1 cm² TiO_x -based cell (control, in blue) and the 1 cm² TiO_xN_y -based cell (in red). The solid and dashed lines represent reverse and forward J - V scans, respectively; schematic of the TiO_xN_y -based cell device structure is plotted in insert figure. Note that the TiO_xN_y ETLs were fabricated at 500°C and all J - V curves of the cells (effective area, 1.2 cm²) were measured using an aperture mask (certified area, 1.0189 cm²). Given that the meso- TiO_2 must be annealed at 500°C to completely remove the organic compounds from the TiO_2 paste, the low temperature (<500°C) processed TiO_xN_y ETLs are not selected for our PSCs in this work. **b**, EQE spectra of the TiO_x -based cell and the TiO_xN_y -based cell. UV-Vis absorption and steady-state PL spectra of the $\text{Cs}_{0.05}\text{FA}_{0.9}\text{MA}_{0.05}\text{PbI}_{2.74}\text{Br}_{0.26}$ film are plotted in insert figure. **c**, FF and PCE distribution for the TiO_x -based cells (12 cells) and the TiO_xN_y -based cells (14 cells). **d**, Schematic representation of the intrinsic (*ex situ*) free electrons of the perovskite, ETL and FTO materials themselves (top left) and the *in situ* free electrons of these different

layers within the perovskite/ETL/FTO layer stack (bottom left); the ETL layer can become fully depleted, and the equilibrium free carrier density falls by orders of magnitude below the ex situ dopant concentration. Schematic diagram of the *ex situ* and *in situ* conductivity of two doping levels of the ETL (right).

METHODS

Materials. Lead iodide (99%), lead bromide (99.999%), Lead chloride (99.999%), Cesium iodide (99.999%), dimethylformamide (DMF, 99.99%), dimethyl sulfoxide (DMSO, 99.99%), poly(methyl methacrylate) (PMMA, MW~120,000), [6,6]-phenyl-C61-butyric-acid-methyl-ester (PCBM, 99.5%), copper phthalocyanine (CuPc, 99%), chlorobenzene (CB, 99.8%), titanium (IV) isopropoxide (TTIP, 99.999%), isopropyl alcohol (IPA, 99.5%), ethyl alcohol (99.5%), hydrochloric acid (HCl, 37%), and indium tin oxide coated glass substrates (ITO, 8-12 Ω /sq) were purchased from Sigma Aldrich. Fluorine doped tin oxide coated glass substrates (FTO, 7 Ω /sq) Formamidinium iodide (FAI), formamidinium bromide (FABr), methylammonium bromide (MABr) and TiO₂ paste (30 NR-D) were purchased from Greatcell Solar. Methylammonium chloride (MACl) was purchased from Xi'an Polymer Light Technology Corp. Poly(3-hexylthiophene) (P3HT) was purchased from 1-Materials. The titanium nitride sputtering target was purchased from AJA International Inc. All chemicals were used as received without further purification.

Preparation of FTO and ITO substrates. The FTO and ITO substrates were sequentially cleaned in detergent, distilled water, acetone, isopropyl alcohol and ethyl alcohol for 20 min in an ultrasonic bath, and then dried with nitrogen. Cleaned FTO and ITO substrates were exposed to approximately 30 min of UV-O₃ treatment before the subsequent deposition step. Note that Sigma Aldrich's ITO product information (<https://www.sigmaaldrich.com/AU/en/product/aldrich/578274?context=product>), says that “ITO coated float glass is only offered with a SiO₂ passivation layer applied directly on the glass prior to ITO coating. The passivation layer is intended to minimize the leaching of alkali oxides into liquid crystals, which can have a detrimental effect on the volume resistivity of the liquid crystal.”

Preparation of nitrogen-doped titanium electron transport layers. First, titanium nitride thin films were deposited on the pre-cleaned FTO (ITO) substrates by radio frequency magnetron sputtering at 300 W and 20 sccm Ar gas using a titanium nitride target under a pressure of 1.5 mTorr. Second, the pre-fabricated titanium nitride thin films were then transferred to a furnace, and annealed at different temperatures ranging from 300°C to 550°C for 45 min under a controlled oxygen atmosphere, where the time of oxygen flow (gas flow ~5 L/min) was fixed at 5 min (Note that the timing was calculated at the beginning of the annealing period). Samples were then cooled to 200°C in the furnace before being removed.

Preparation of solution-processed titanium oxide electron transport layers. ~50 nm compact TiO_x thin films were deposited on the pre-cleaned FTO (ITO) substrates according to our previous work¹⁵, where the compact TiO_x precursor solution contained 369 µL TTIP and 35 µL 2 M HCl in 5 mL anhydrous IPA.

Preparation of mesoporous titanium oxide scaffold layers. ~40 nm mesoporous TiO₂ scaffold layers were deposited on the FTO/TiO_xN_y or FTO/TiO_x substrates according to our previous work⁵, where the mesoporous TiO₂ precursor solution was prepared from 30 nm TiO₂ paste diluted in ethyl alcohol (1:9, w/w). All samples were annealed at 500°C for 30 min under dry air.

Preparation of precursor solution. The Cs_{0.05}FA_{0.9}MA_{0.05}PbI_{2.74}Br_{0.26} perovskite precursor solution contains 0.065 M CsI, 1.15 M PbI₂, 0.11 M PbBr₂, 1.1 M FAI, 0.045 M FABr, 0.065 M MABr, 0.01 M PbCl₂, 0.01 M MACl in 1 mL anhydrous DMF:DMSO (4:1, v/v). PMMA:PCBM⁵ passivation precursor solution was prepared by dissolving 0.5 mg PMMA and 1.5 mg PCBM into 1 mL CB. PMMA⁵ passivation precursor solution was prepared by dissolving 0.25 mg/mL PMMA in CB. P3HT:CuPc⁸ hole transport layer precursor solution was prepared with a 10:1 (v/v) ratio blend of P3HT (12 mg/mL in CB):CuPc (5 mg/mL in CB).

Device fabrication. For the ultra-thin passivation layer deposition, ~100 µL PMMA:PCBM precursor solution was dropped onto the FTO/TiO_xN_y (or TiO_x)/meso-TiO₂ substrates and deposited by spin-coating at 5000 rpm/s with a ramp of 5000 rpm s⁻¹ for 30 s, then annealed at 100°C for 10 min. Cs_{0.05}FA_{0.88}MA_{0.07}PbI_{2.56}Br_{0.44} thin films were then deposited on the passivated substrates by a two-step spin coating program: first at 2000 rpm with a ramp of

200 rpm s⁻¹ for 10 s, and then at 4000 rpm with a ramp of 1000 rpm s⁻¹ for 20 s. The perovskite precursor film was immediately transferred into a custom-built vacuum flash³⁶ system where a two-step vacuum procedure was applied: first, the system was immediately pumped down to a low pressure of ~100 mTorr and held for 20 s; the pressure was then increased to ~1.2 Torr and held for another 10 s. The pump valve was then turned off and left to return to atmospheric pressure. After the vacuum flash treatment, the perovskite sample was immediately annealed on a hotplate at 100°C for 120 s. The sample was then returned to the spin-coater and cooled down by fast rotation at 5000 rpm with a ramp of 5000 rpm s⁻¹ for 60 s. Next, the PMMA passivation treatment was applied: first, ~100 uL PMMA solution (0.25 mg/ml in Chlorobenzene) was dropped onto the perovskite sample and left for 2 s; second, the sample was spin-coated for 15 s at 5000 rpm with a ramp of 5000 rpm s⁻¹; finally, the sample was annealed on a hotplate at 100°C for 60 min. The P3HT:CuPc hole transport layer was deposited via spin coating at 2000 rpm with a ramp of 500 rpm s⁻¹ for 30 s. Finally, ~100 nm gold was deposited through a shadow mask (cell area 1.2 cm²). All depositions were conducted in a nitrogen-filled glovebox.

Solar cell characterisation. All devices were tested under 1 sun conditions (100 mW/cm², AM 1.5G) in a solar simulator system (Wavelab Inc.). The light intensity was calibrated using a certified Fraunhofer CalLab reference cell. All *J-V* curves were measured at a 20 mV/s scan rate with an aperture mask (certified area is ~1.0189 cm²) in a custom-built measurement jig under nitrogen flow. Note that reverse scan is from *V*_{OC} to *J*_{SC} (forward bias → short circuit, 1.2 V → -0.1 V), and forward scan is from *J*_{SC} to *V*_{OC} (short circuit → forward bias, -0.1 V → 1.2 V). External quantum efficiency (EQE) was measured using DC measurement module on a commercial EQE system (CEP-25ML, Bunkoukeiki). For the TiO_xN_y perovskite cell, the estimated spectrum mismatch correction is 98.36% based on the comparison between the integrated current density calculated from the EQE response and the current density measured under the solar simulator. No preconditioning protocol was applied before the characterisation.

The performance distribution of TiO_xN_y-based PSCs fabricated with ITO substrates is shown in Supplementary Fig. 3. The average PCE of TiO_xN_y cells is 22.78% ± 0.17% (champion PCE ~ 23.09%) with FF ~ 0.842 ± 0.006 (champion FF ~ 0.849), while that of TiO_x ('Control') cells is 21.03% ± 0.27% (champion PCE ~ 21.47%) with FF ~ 0.785 ± 0.012 (champion FF ~ 0.802). Note that the performance of ITO-based TiO_xN_y or TiO_x cells is lower than that of the corresponding FTO-based TiO_xN_y or TiO_x cells. This is because the

sheet resistance of ITO substrates (initially 8-10 Ω/sq) increases to ~26-30 Ω/sq when annealed at 500°C for 30 min, while that of FTO substrates (~7 Ω/sq) does not change. For this reason, the slightly decreased performance of ITO-based cells originates from the increased sheet resistance of the ITO substrates.

Damp-heat test. The damp-heat (85°C, 85% relative humidity) tests under dark were performed using a climate test chamber (Weiss Technik). When measuring the cells during the aging, samples were removed from the chamber and allowed to cool down to room temperature. Note that the perovskite cells used for the damp heat tests included an additional barrier layer deposited on the HTL before the gold electrode. The barrier layer consisted of ~10 nm MoO_x deposited by thermal evaporation followed by ~40 nm of IZO deposited by sputtering. The function of the MoO_x was to prevent sputtering damage to the underlying HTL. The rest of the cell fabrication was identical to the process described above. Cells were then encapsulated between two pieces of glass and the edges were sealed with polyisobutylene³⁷.

Film characterisation. The top-morphology of bare FTO and $\text{FTO}/\text{TiO}_x\text{N}_y$ samples was imaged with a non-contact tapping mode atomic force microscope (AFM, Asylum research). X-ray photoelectron spectroscopy (XPS) and ultraviolet photoelectron spectroscopy (UPS) measurements were carried out on an XPS machine (Escalab 250 Xi, Thermo Fisher), with a monochromatic $\text{Al K}\alpha$ (1486.7 eV) X-ray source for XPS and a He I (21.2 eV) gas discharge lamp for UPS. The detailed XPS peak analysis is presented below.

As shown in Fig. 1a, the Ti^{2+} oxidation state is present in the as-deposited TiN film, with the Ti 2p peaks centered at binding energies of ~456.1 eV and ~461.6 eV²¹. In addition, the O 1s XPS peak indicates the presence of a significant amount of O even in the as-deposited sample (Fig. 1b). This might be caused by the natural oxidation of the TiN sputtering target during storage or by oxidation from residual oxygen in the chamber during the sputtering process. For the '300 C' sample, the Ti 2p core-level peaks are at binding energies of ~457.1 eV and ~458.6 eV/~464.4 eV, which can be respectively ascribed to Ti^{3+} and Ti^{4+} oxidation states^{15,21}, indicating that the TiN starts oxidising at 300°C under oxygen atmosphere. Both the TiN and Ti^{2+} peaks vanish when annealed at 350°C, while the Ti^{3+} peaks reduce when the annealing temperature is increased from 350°C to 400°C. There is no evidence of Ti^{3+} peaks in films annealed at 450°C and above.

For the O 1s XPS spectra (Fig. 1b), the dominant peaks at all temperatures are centered at binding energies of ~530.1 eV to ~530.5 eV which we attribute to titanium oxides (TiO_x)^{15,22}, while the smaller peaks at higher binding energies of ~532.0 eV can be assigned to hydroxyl groups or O_2 ^{15,22}.

As shown in Fig. 1c, the N 1s core level peak of the ‘as-deposited’ sample could be deconvoluted into three different N species. The peak centred at ~397.2 eV binding energy and its satellite are indicative of TiN ^{18,23}; while the smaller peak centred at a lower binding energy of ~396.5 eV can be allocated to O-Ti-N^{18,23,24}, suggesting the oxidation state of Ti is present in the as-deposited TiN film. This oxidised TiN, i.e. O-doped TiN_y , is the early stage of TiO_xN_y .

The relative height of the O-Ti-N peak increases when oxidised at 300°C and becomes the dominant N 1s peak at 350°C. A new peak centred at a higher binding energy of ~402 eV is observed for the ‘350 C’ sample, which we attribute to chemisorbed nitrogen, also denoted as $\gamma\text{-N}_2$ ^{23,26}. In addition, the TiN peak vanishes when annealed at 350°C, consistent with the Ti 2p core-level peak analysis (see Fig. 1a). Therefore, the 350°C oxidised film is dominated by N-doped TiO_x (see Extended data Fig. 2). Note that the slight shift of the O-Ti-N peak to a lower binding energy of ~396.2 eV might be caused by the transition of the dominant chemical state of TiO_xN_y from O-doped TiN_y to N-doped TiO_x .

For the ‘400 C’ sample, a new peak is observed at a binding energy of ~400 eV, which can be ascribed to the NO_x functional group^{18,23,25}. For this sample the peak intensity of O-Ti-N decreases and the $\gamma\text{-N}_2$ peak shifts to a slightly higher binding energy of ~403 eV. This is because the oxidation states of Ti within the ‘400 C’ sample are dominated by Ti^{4+} (Fig. 1a) and O-rich N-doped TiO_x lattices are formed after annealing at 400°C (see Extended data Fig. 2). Note that the O-Ti-N peak cannot be detected for TiO_xN_y films annealed at 450°C and above.

In general, for non-metal-doped TiO_x , substitutional doping of the O lattice site is preferred in O-deficient conditions while interstitial doping is favoured in O-rich conditions¹⁸. Here, the O-Ti-N species in N 1s core-level peaks is associated with both O substitutional doping in TiN_y or N substitutional doping in TiO_x lattices; while the NO_x peaks can be attributed to N interstitial doping in O-rich TiO_x lattices^{18,23,25}.

The TiO_xN_y lattices will be eventually oxidised into pure TiO_x lattices with further increasing the annealing temperature (>550°C) as the reaction of oxidation of TiN to TiO_2 is thermodynamically favourable^{18,30}, where the relevant chemical reaction equation is $\text{TiN} + \text{O}_2 \rightarrow \text{TiO}_2 + 1/2 \text{N}_2$.

UV-Vis transmittance and absorption spectra were measured using a PerkinElmer Lambda 1050 UV/Vis/NIR spectrophotometer. A FEI Verios scanning electron microscope (SEM) and a Helios Nanolab 600 FIB system were used to investigate the surface morphology and cross-sectional SEM images of the perovskite samples, respectively. The transmission electron microscopy (TEM) measurements were performed in a JEOL 2100F operating at 200 keV. The simulation of the polycrystalline TEM diffraction patterns was performed using the JEMS³⁸ code as implemented on version 4.6131U2018.

36. Ding, B. et al. Facile and scalable fabrication of highly efficient lead iodide perovskite thin-film solar cells in air using gas pump method. *ACS Appl. Mater. Interfaces* **8**, 20067-20073 (2016).

37. Shi, L. et al. Accelerated lifetime testing of organic-inorganic perovskite solar cells encapsulated by polyisobutylene. *ACS Appl. Mater. Interfaces* **9**, 25073-25081 (2017).

38. Stadelmann, P. A. EMS - a software package for electron diffraction analysis and HREM image simulation in materials science. *Ultramicroscopy* **21**, 131-145 (1987).

Acknowledgments

This work was supported by the Australian Government through the Australian Renewable Energy Agency (ARENA) and the Australian Research Council. Responsibility for the views, information or advice expressed herein is not accepted by the Australian Government. J. P. acknowledges the financial support of a Postdoc Fellowship from the Australian Centre for Advanced Photovoltaics (ACAP). T. P. W. is the recipient of an Australian Research Council Future Fellowship (project number FT180100302) funded by the Australian Government. T.P.W also acknowledges the support of the Open Fund of the State Key Laboratory of Optoelectronic Materials and Technologies (Sun Yat-sen University). D. Z. acknowledges funding from the National Natural Science Foundation of China (grant Nos. 11574403, 11974431). The work was partly conducted at the ACT node of the Australian National Fabrication Facility (ANFF), and the ANU node of the Australian Microscopy and Microanalysis Facility (AMMRF). We thank Dr. Sachin Surve and Mr. Shenyao Zhao for experimental assistance.

Author contributions

J. P. conceived the idea, designed the overall experiments and led the project. J. P. optimised the sputtered TiO_xN_y thin films. J. P. and Y. W. prepared and characterised the perovskite cell

devices. F. K. and F. B. performed the TEM measurements and analysis. D. W., T. P. W. and K. J. W. conducted the device numerical simulation. Y. J. and J. X. performed the XPS/UPS measurements and analysis. D. Z. supervised the XPS/UPS measurements and analysis. Y. W. performed the Hall-Effect measurements and analysis. W. L. performed the EQE measurements. T. L. and Y. L. performed the AFM measurements. T. D. and H. S. performed the steady-state and time-resolved PL, UV-Vis transmittance and absorption measurements. L. L. and O. L. C. L. conducted the SEM measurements. K. R. C. and T. P. W. supervised the project. J. P. wrote the manuscript. All authors contributed to the discussion of the results and revision of the manuscript.

Competing interests

The Australian National University has filed a patent related to the subject matter of this manuscript.

Data availability

The data that support the findings of this study are available from the corresponding authors on reasonable request.

Additional Information

Extended data and Supplementary Information are available for this paper.

Correspondence and requests for materials should be addressed to J. P. or T. P. W. or K. R. C.

Extended Data Fig. 1 | Surface morphology characterisation by AFM. **a**, Bare FTO substrate. **b**, FTO/TiN substrate without post-annealing treatment (labeled as ‘As-deposited’). **c**, FTO/TiO_xN_y substrate annealed at 300°C (labeled as ‘300 C’). **d**, FTO/TiO_xN_y substrate annealed at 350°C (labeled as ‘350 C’). **e**, FTO/TiO_xN_y substrate annealed at 400°C (labeled as ‘400 C’). **f**, FTO/TiO_xN_y substrate annealed at 450°C (labeled as ‘450 C’). **g**, FTO/TiO_xN_y substrate annealed at 500°C (labeled as ‘500 C’). **h**, FTO/TiO_xN_y substrate annealed at 550°C (labeled as ‘550 C’). Note that the legend of ‘RMS’ represents root mean square of the surface roughness.

Extended Data Fig. 2 | XPS element analysis. The atomic ratio of O to Ti and N to Ti for TiO_xN_y thin films annealed at different temperatures.

Extended Data Fig. 3 | TEM characterisation. **a**, TiO_xN_y without annealing ('As-deposited'). **b**, TiO_xN_y annealed at 300°C. **c**, TiO_xN_y annealed at 400°C. **d**, TiO_xN_y annealed at 500°C.

Extended Data Fig. 4 | TEM characterisation and simulation of the diffraction pattern. **a** and **b**, TiO_xN_y annealed at 350°C. **c** and **d**, TiO_xN_y annealed at 450°C. **e** and **f**, TiO_xN_y annealed at 550°C. Note that the non-continuous diffraction ring visible in Fig. 4f diffraction pattern is caused by the low crystal density within the specimen.

Extended Data Fig. 5 | Optical bandgap characterisation. Tauc plots for the as-deposited TiN film and TiO_xN_y films annealed at different temperatures. Note that all films (~50 nm) were deposited on quartz substrates.

Extended Data Fig. 6 | Device structure. **a**, The cross-sectional SEM image of the TiO_xN_y -based cell with a structure of glass/FTO/ TiO_xN_y (~40 nm)/meso- TiO_2 (~50 nm)/ultrathin PMMA:PCBM (<3nm)/Perovskite (~500 nm)/ultrathin PMMA (<3 nm)/P3HT:CuPc (~65 nm)/Gold. **b**, The cross-sectional SEM image of the TiO_x -based cell with a structure of glass/FTO/ TiO_x (~50 nm)/meso- TiO_2 (~50 nm)/ultrathin PMMA:PCBM (<3 nm)/Perovskite (~500 nm)/ultrathin PMMA (<3 nm)/P3HT:CuPc (~65 nm)/Gold. Note that the meso- TiO_2 and perovskite represent mesoporous TiO_2 and $\text{Cs}_{0.05}\text{FA}_{0.9}\text{MA}_{0.05}\text{PbI}_{2.74}\text{Br}_{0.26}$, respectively.

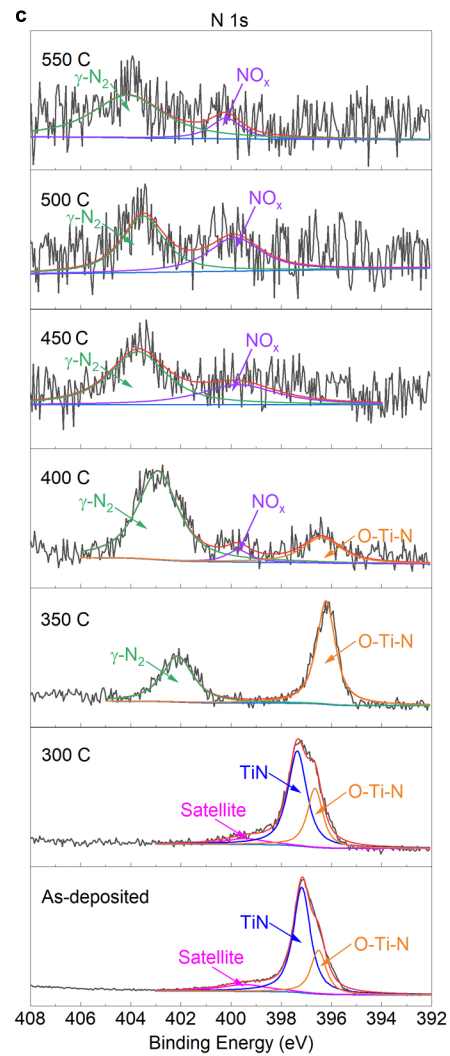
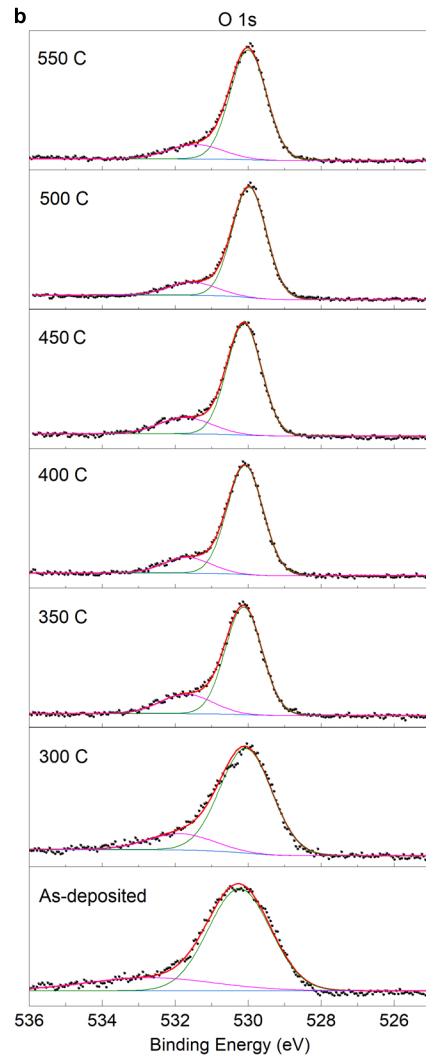
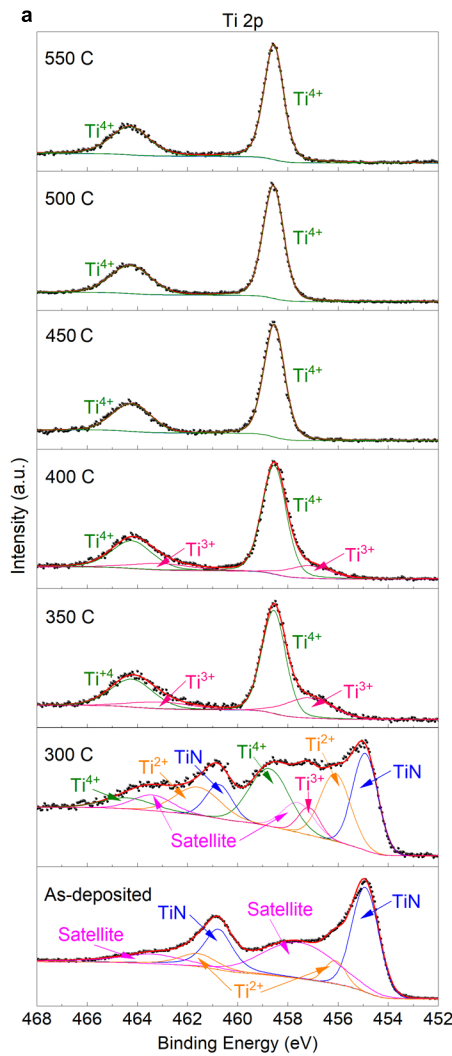
Extended Data Fig. 7 | Device characterisation. **a**, V_{OC} and J_{SC} distribution for the TiO_x -based cells (12 cells) and the TiO_xN_y -based cells (14 cells). **b**, The J - V curve of the perovskite cells based on the TiO_xN_y ETLs, which were annealed at 550°C. **c**, The J - V parameters distribution of the TiO_xN_y (annealed at 550°C) based cells (15 cells).

Extended Data Fig. 8 | Effects of electron transport layers with different carrier densities on the performance of perovskite solar cells. **a**, Simulated J - V curves where only ETL doping is varied using dopant densities taken from Hall effect measurements. **b**,

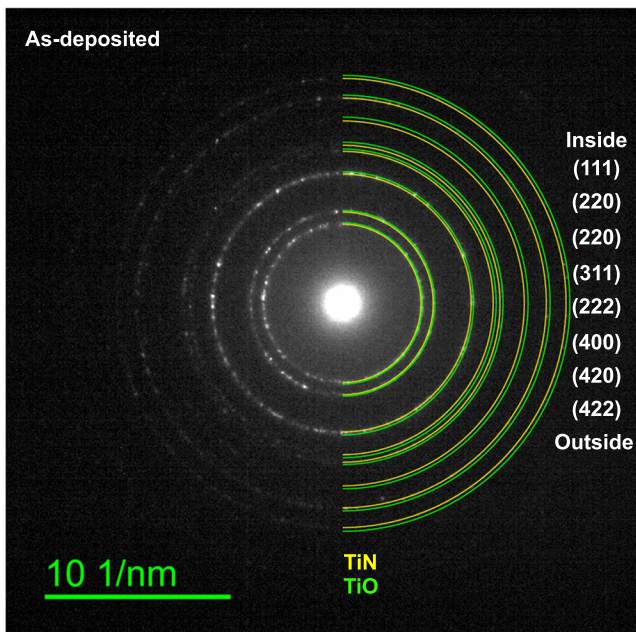
Experimental J - V curves for the reference TiO_x and TiO_xN_y PSCs. Reduction in FF and increase in Ohmic series resistance is predominantly due to electron depletion in the ETL layer. **c**, Energy level diagram of electron quasi-Fermi levels and conduction band, illustrating the resistive voltage loss in the ETL for the lowly-doped cases. Note that Energy levels and electron concentrations at 22.5 mA/cm^2 for ETLs with doping densities equivalent to TiO_x ($5 \times 10^{14} \text{ cm}^{-3}$) and TiO_xN_y ($3 \times 10^{17} \text{ cm}^{-3}$). **d**, Electron concentration in the ETL for doping levels from $5 \times 10^{14} - 10^{18} \text{ cm}^{-3}$. Note that the dash-dot horizontal lines mark the dopant defect concentration, indicating the magnitude of electron depletion. With the exception of extremely high doping at 10^{18} cm^{-3} , in no case does the free electron concentration reach even the same order of magnitude as the fixed dopant concentration. **e-f**, Contour plots of perovskite solar cell fill factor (**e**) open-circuit voltage (**f**) across a range of ETL doping levels and electron affinity. Note that the stars mark the conditions simulated in Fig. 9a. The vertical dashed lines mark the doping levels of the TiO_x and optimized TiO_xN_y films fabricated in this work. Electron depletion from the ETL suggests that high doping is in general necessary to achieve fill factors on the order of 85% or above.

Extended Data Fig. 9 | Device stability characterisation. a, Light-soaking stability tests. **b**, Damp-heat stability tests. Note that SPO represents steady-state power output measured by maximum power point voltage (V_{MPP}) tracking under continuous 1 sun illumination intensity. The device structure of the encapsulated cells is glass/FTO/ TiO_xN_y (or TiO_x)/m- TiO_2 /PMMA:PCBM/Perovskite/PMMA/P3HT:CuPc/MoO_x (~10 nm)/IZO (~40 nm)/Au, where the perovskite is $\text{Cs}_{0.05}\text{FA}_{0.9}\text{MA}_{0.05}\text{PbI}_{2.74}\text{Br}_{0.26}$. Details of encapsulation are provided in the experimental section.

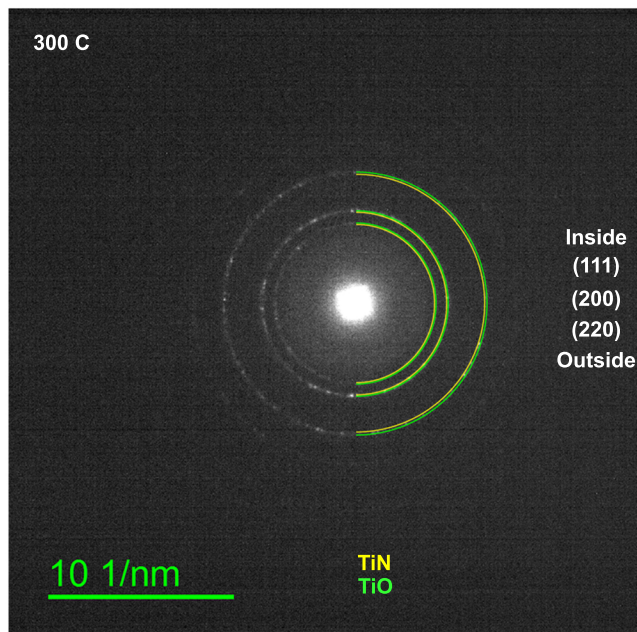
Extended Data Table 1 | Summarised parameters for the Hall-effect measurements.



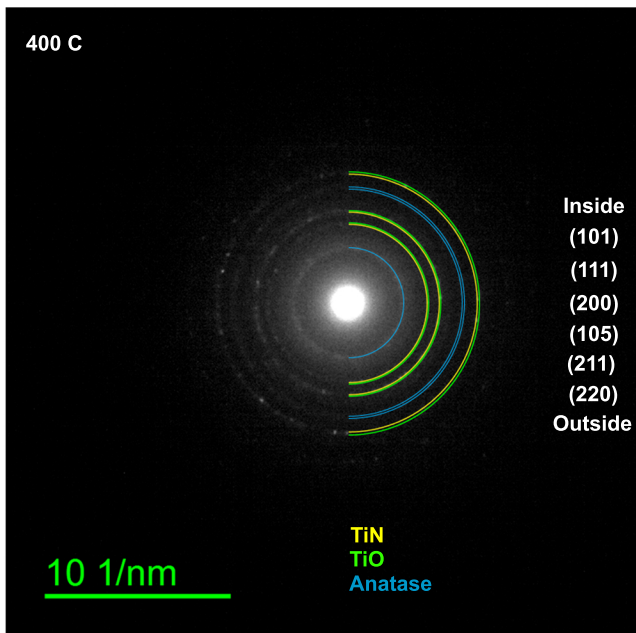
a



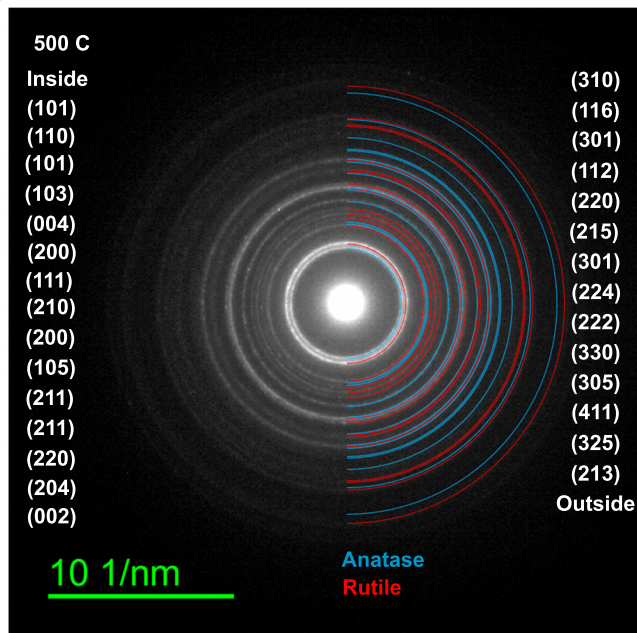
b

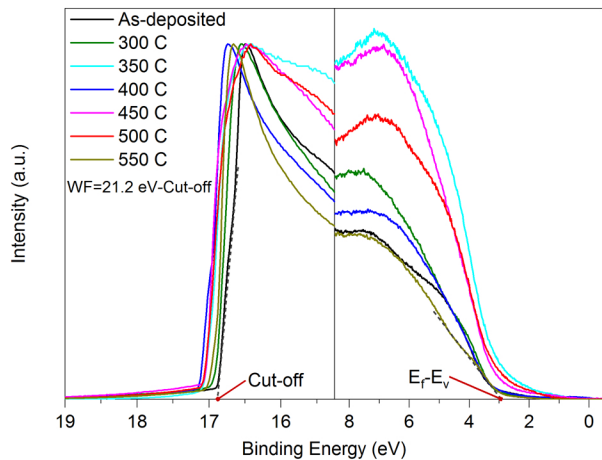
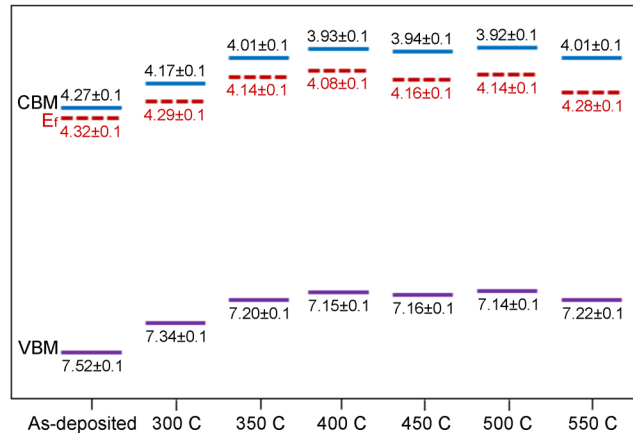
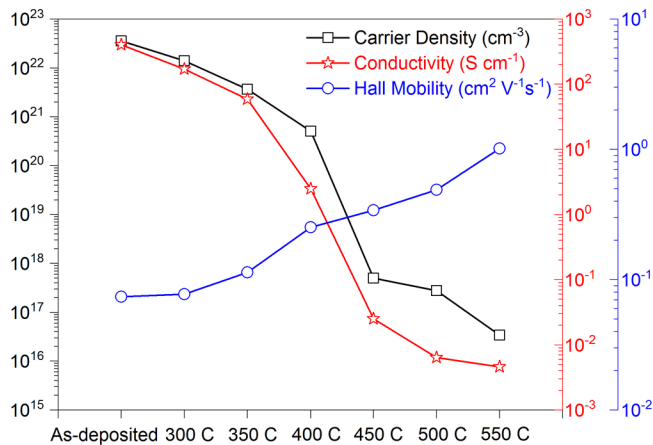


c



d



a**b****c****d**